Scientific Research Publishing

Materials Sciences and Applications, 2023, 14, 299-323
https://www.scirp.org/journal/msa
ISSN Online: 2153-1188
ISSN Print: 2153-117X

A Comprehensive Review of Experience with the Application of the Mechanical Threshold Stress Model

Paul S. Follansbee

Professor Emeritus, Engineering Department, Saint Vincent College, Latrobe, Pennsylvania, USA
Email: paul.follansbee@stvincent.edu

How to cite this paper: Follansbee, P.S. (2023) A Comprehensive Review of Experience with the Application of the Mechanical Threshold Stress Model. *Materials Sciences and Applications*, **14**, 299-323.
https://doi.org/10.4236/msa.2023.145019

Received: March 28, 2023
Accepted: May 28, 2023
Published: May 31, 2023

Abstract

Accurate prediction of stress-strain behavior of metals as a function of arbitrary temperature and strain rate paths has remained a challenge. The Mechanical Threshold Stress constitutive model is one formalism that has emerged following several decades of research. Vast experience has accumulated with the application of the Mechanical Threshold Stress model over a wide variety of pure metals and alloys. Out of this has arisen common trends across metal systems. The magnitude of activation energies presents one example of this, where these variables consistently increase in magnitude as the obstacle to dislocation motion transitions from short range to long range. Trends in strain hardening are also observed. In Face-Centered Cubic metals the magnitude of strain hardening scales with the stacking fault energy; trends in Body-Centered Cubic metals are less clear. Model parameters derived for over twenty metals and alloys are tabulated. Common trends should guide future application of the MTS model and further model development.

Keywords

Mechanical Threshold Stress, Constitutive Behavior, Deformation Kinetics, Strain Hardening, Internal State Variable

1. Introduction

The Mechanical Threshold Stress (MTS) constitutive formulation is an internal-state variable model that computes stress as the sum of the contributions from individual obstacles to dislocation motion [1] [2] [3]. These contributions are characterized by the threshold stress $\hat{\sigma}$ that is the stress at 0 K required to

promote dislocation motion past the particular obstacle. Obstacle populations include solutes, precipitates, the Peierls barrier in Body-Centered Cubic metals, and other dislocations, e.g., stored dislocations. This section provides a brief review of the theory and operative equations that comprise the MTS model.

The most general expression for the yield stress as a function of temperature and strain rate is

$$\frac{\sigma}{\mu}=\frac{\sigma_a}{\mu}+\sum_1^n s_i\left(\dot{\varepsilon},T\right)\frac{\hat{\sigma}_i}{\mu_o} \tag{1}$$

where σ_a is an athermal stress, due for instance to the contribution of the interaction of grain boundaries, $\hat{\sigma}_i$ is the threshold stress for obstacle population i, s_i is a factor between 0 and 1 that characterizes the influence of temperature and strain rate on the stress required to overcome the obstacle, μ is the shear modulus, μ_o is the shear modulus at 0 K, and n is the number of obstacle populations contributing to the stress. A general form for s_i follows from work of Kocks *et al.* [4]:

$$s_i\left(\dot{\varepsilon},T\right)=\left\{1-\left[\frac{kT}{g_{oi}\mu b^3}\ln\left(\frac{\dot{\varepsilon}_{oi}}{\dot{\varepsilon}}\right)\right]^{1/q_i}\right\}^{1/p_i} \tag{2}$$

where T is the test temperature, $\dot{\varepsilon}$ is the test strain rate, b is the Burgers vector, k is Boltzmann's constant, g_{oi} is the normalized activation energy, and $\dot{\varepsilon}_{oi}$, q_i, and p_i are constants. These last four variables are specific to the obstacle population (i) of interest, although as will be shown, these variables show common trends. Equation (1) and Equation (2) specifically apply to the yield stress in annealed metals. These equations are referred to as the "Yield Stress" Kinetics analysis (YSA).

In deformed metals, Equation (1) is written as

$$\frac{\sigma}{\mu}=\frac{\sigma_a}{\mu}+\sum_1^n s_i\left(\dot{\varepsilon},T\right)\frac{\hat{\sigma}_i}{\mu_o}+s_\varepsilon\left(\dot{\varepsilon},T\right)\frac{\hat{\sigma}_\varepsilon}{\mu_o} \tag{3}$$

where a threshold stress term $\hat{\sigma}_\varepsilon$ arising from the contribution of mobile dislocations with stored dislocations is added (with its associated s-value). A recent paper has addressed the challenge of applying Equation (3) to a material supplied with an existing dislocation density from, for instance, a final warm working operation [5].

Application of the MTS model to a variety of Body-Centered Cubic (BCC), Face-Centered Cubic (FCC), and Hexagonal Close Packed (HCP) metals as well as to austenitic stainless steels and superalloys has been thoroughly reviewed [2]. Section 2 through Section 5 summarize trends observed in these analyses. In particular assessed values of the normalized activation energies (Equation (2)) and mechanical threshold stresses (Equation (1)) are compared and displayed in several tables.

Equation (3) introduced an additional mechanical threshold stress $\hat{\sigma}_\varepsilon$. The increase of $\hat{\sigma}_\varepsilon$ with strain results from the rising difficulty of moving disloca-

tions through the array of stored dislocations. This process is referred to as "evolution", which is used interchangeably with the term "strain hardening". The increase of $\hat{\sigma}_{\varepsilon}$ with strain is described differentially, using a modified Voce equation:

$$\frac{\mathrm{d}\hat{\sigma}_{\varepsilon}}{\mathrm{d}\varepsilon} = \theta_{II}\left(\dot{\varepsilon}\right)\left(1-\frac{\hat{\sigma}_{\varepsilon}}{\hat{\sigma}_{\varepsilon s}\left(\dot{\varepsilon},T\right)}\right)^{\kappa} \tag{4}$$

where θ_{II} is the stage II hardening rate, e.g., of a single crystal, $\hat{\sigma}_{\varepsilon s}$ is the saturation value of this threshold stress and κ is a constant, usually equal to one or two. Note that the saturation threshold stress has a temperature and strain-rate dependence. This is unique from that defined for the stress in Equation (1) and Equation (2). The kinetics are specified by a dynamic recovery model proposed by Kocks. [6]

$$\ln\hat{\sigma}_{\varepsilon s} = \ln\left(\hat{\sigma}_{\varepsilon so}\right) + \frac{kT}{\mu b^{3}\left(g_{\varepsilon so}\right)}\ln\frac{\dot{\varepsilon}}{\dot{\varepsilon}_{\varepsilon so}} \tag{5}$$

where $\hat{\sigma}_{\varepsilon so}$ is the saturation stress at 0 K, $g_{\varepsilon so}$ is the applicable normalized activation energy, and $\dot{\varepsilon}_{\varepsilon so}$ is a constant. Equation (4) and Equation (5) are referred to as the "Evolution" Kinetics Analysis (EA).

Section 6 reviews trends in the parameters $\hat{\sigma}_{\varepsilon so}$, k, and $g_{\varepsilon so}$ across several metals and alloys. These trends are displayed both graphically and in tabular form. The unique contribution of this paper is in the description of common trends in both the Yield Stress Kinetics analysis (YSA) and the Evolution Kinetics Analysis (EA) that could guide application of the MTS model to other metals and alloys. Inspection of the operative equations introduced above indicates a number of model variables. One objective of this paper is to specify ranges for many of these variables and to conclude with a listing of the independent variables in the MTS formalism (see Appendix).

2. Application of the YSA When Two Strengthening Mechanisms Are Active

One of the challenges in applying the model is the selection of the operative strengthening mechanisms, which defines the number n in Equation (1). In a pure metal, such as 0.9999 Cu, n may equal 0. That is, there is no strengthening contribution from solutes in this highly pure metal. In most FCC metals, the strengthening from solute additions, whether intentional or not, can be significant. However, the strengthening contributions of all of the impurities are difficult to assess. For most of the metals and alloys analyzed, it has been assumed that n equals 2; that is, two strengthening mechanisms are dominant. Under this assumption, Equation (1) becomes

$$\frac{\sigma}{\mu} = \frac{\sigma_{a}}{\mu} + \mathrm{s}_{1}\left(\dot{\varepsilon},T\right)\frac{\hat{\sigma}_{1}}{\mu_{o}} + \mathrm{s}_{2}\left(\dot{\varepsilon},T\right)\frac{\hat{\sigma}_{2}}{\mu_{o}}. \tag{6}$$

Note that nowhere has it been firmly established that the contributions from

the two obstacle populations sum linearly. This question was addressed by Follansbee and Gray in the Ni-C system [7] where the fit using Equation (6), or more simply

$$\sigma = \sigma_1 + \sigma_2 \tag{7}$$

was compared to that using

$$\sigma = \sqrt{\sigma_1^2 + \sigma_2^2}\ . \tag{8}$$

The conclusion was that there was no improvement in the agreement with data using Equation (8) rather than Equation (7). Going forth, the linear summation of individual stress components has been assumed.

In the BCC systems, obstacle population 1 was assumed to be the Peierls barrier [8]. This is characterized by very short-range dislocation interactions with a low value of g_{o1} (or g_{op}). The term "short-range" relates to the area swept out by the dislocation as it encounters an obstacle [4]. A second strengthening contribution was assumed to arise from dislocation interactions with impurity atoms. These were longer-range interactions with a moderate value of g_{o2} (or g_{oi}). Some FCC and HCP systems were adequately assessed using a single strengthening contribution, presumably from solute interactions, again characterized by a moderate value of g_{oi}. Several others, as described in a following section, were better described using two strengthening mechanisms.

It is very difficult to ascertain which solute-dislocation interaction is responsible for the observed strengthening. In the Ni-C system [7], the alloys were specifically supplied with three different carbon concentrations. The highest concentration was 1900 parts per million (ppm) C, which is well above the trace amounts of other elements, which are typically less than 200 ppm. The effect of C on strengthening in Fe is well known, as is the effect of O and Al on the strengthening in Ti. But in other systems, there may be numerous elements with small, but similar, concentration levels. In these metals, there may be insufficient information on strengthening due to a specific solute, and the validity of the approximation that these all can be described using a single solute strengthening mechanism is unknown.

For example, the chemical analysis of the molybdenum studied by Briggs and Campbell [9] reported 14 ppm O, 12 ppm N, 10 ppm Fe, 70 ppm Si, 100 ppm W, and trace amounts of H and Cu. The analysis published by Follansbee [8] proceeded with a 2-obstacle population model. Clearly the Peierls barrier is one of these; the other represents the contributions of dislocation interactions with the impurity elements. It is an approximation to assume these can all be lumped into a single threshold stress $\hat{\sigma}_i$ with a single value of g_{oi}. However, there is insufficient information to do otherwise. This would require an experimental campaign with intentionally variable solute additions. That is, molybdenum alloys with 30 ppm O, 50 ppm O, and 70 ppm O with all other elements unchanged, might yield information about the specific role of O in strengthening. This would indeed be an extensive campaign.

3. Extracting YSA Model Constants from Data Sets

In this section, the procedure to extract the model parameters $\hat{\sigma}_i$ and g_{oi} will be reviewed. One starts with a collection of stress-strain measurements as a function of test temperature and strain rate. These measurements should be in a material that is in the annealed condition with a low starting dislocation density. The focus here is on the yield stress. Analysis of the hardening behavior generally follows. With knowledge of the Burgers vector and the temperature-dependent shear modulus [2] (pp. 136-137)[1], the yield stresses are plotted according to Equation (1) with $n = 1$, when a single strengthening mechanism applies, or $n = 2$ when two strengthening mechanisms apply. **Figure 1** shows the measurements of Briggs and Campbell [9] which cover a strain rate range from 1.7×10^{-4} s^{-1} to 100 s^{-1} and temperatures from 77 K to 600 K. Note that the plot exhibits a distinct curvature. This suggests that a two-parameter analysis is in order. Since this is a BCC metal, the Peierls barrier serves as one of the obstacle populations. The net effect of the, albeit low, concentration of impurities (the chemical concentration detailed above translates to a purity level of 0.9996) likely contributes to the second obstacle population. The procedure requires the analyst to select values of $\hat{\sigma}_p$, g_{op}, $\hat{\sigma}_i$, and g_{oi} that provide a good fit with the measurements. **Figure 2** shows the derived model fit along with the measurements. For this fit, of $\hat{\sigma}_p$ = 1541 MPa, $g_{op} = 0.07$, $\hat{\sigma}_i$ = 428 MPa, and $g_{oi} = 0.27$. As expected, the Peierls barrier, with a low g_o value and a high threshold stress, dominates. The strengthening contribution due to the impurities is much less and the g_o value suggests this is a longer-range dislocation-obstacle interaction. The temperature-dependence demonstrated by the Peierls barrier is quite high; in fact, its contribution goes to zero at ~500 K. (This is somewhat strain-rate dependent; at higher strain rates this strengthening contribution would persist to higher temperatures.)

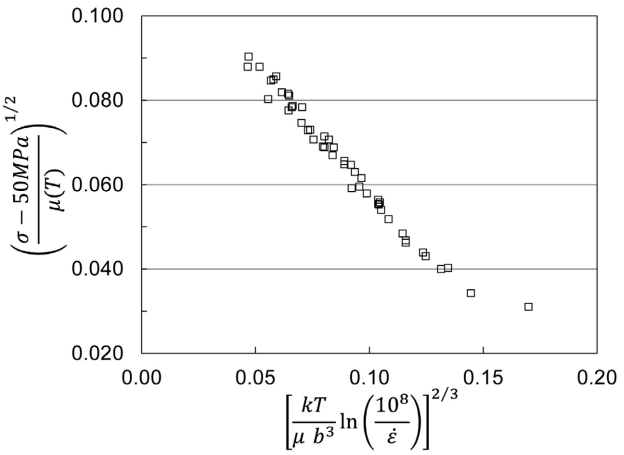

Figure 1. Briggs and Campbell measurements [5] [9] in pure molybdenum analyzed according to Equation (6) and Equation (2).

[1]To assist the reader, many of the following references to [2] include the table (T), figure (F), or page number(s).

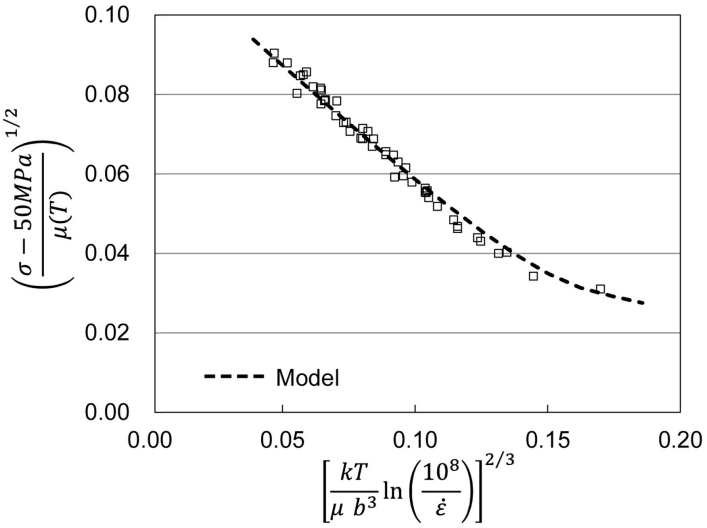

Figure 2. Briggs and Campbell measurements [5] [9] in pure molybdenum along with the two-obstacle population model fit.

Figure 3 shows the analysis of yield stress measurements in pure Zinc. Measurements reported by Risebrough in 99.999% pure material with a grain size of 20 μm [10] and measurements reported by Liu, Huang, Wu, and Zhang in material with the same purity but with a grain size of 70 μm [11] are plotted on the same coordinates used in **Figure 1** and **Figure 2**. Because of the large grain size difference, a lower value of σ_a (5 MPa) was used for the Liu *et al.* analysis than for the Risebrough analysis (10 MP). In this case, the data fall nicely along a straight line, suggesting that one strengthening mechanism is operative; this strengthening is likely due to interaction of dislocations with impurity elements. The analysis yielded $\hat{\sigma}_i$ = 181 MPa, and g_{oi} = 0.17.

YSA Cases Where Assuming a Two-Obstacle Model Can Be Misleading

To demonstrate a case where assuming a two-obstacle model can be misleading, a fictitious alloy was created using the parameters b, σ_a, $\mu(T)$, etc. defined for Follyalloy [2] [5]. **Figure 4(a)** gives the yield stress versus temperature and strain rate plot for this alloy. The model shown is a two-obstacle analysis with $\hat{\sigma}_p$ = 2500 MPa, g_{op} = 0.19, $\hat{\sigma}_i$ = 530 MPa, and g_{oi} = 4.2. A red flag immediately rises with the high value of g_{oi}, which is an unusually high activation energy.

Figure 4(b) shows the same data set. In this case the model is a four-obstacle analysis with the model parameters shown in **Table 1**. Included in this table are the model parameters for the two-obstacle model. Interestingly, the fit to the data set is only slightly better in the four-obstacle analysis than in the two-obstacle analysis. The error, defined

$$\text{Error} = \left\{\sum\left(\sigma_m - \sigma\right)^2\right\}^{1/2} \tag{9}$$

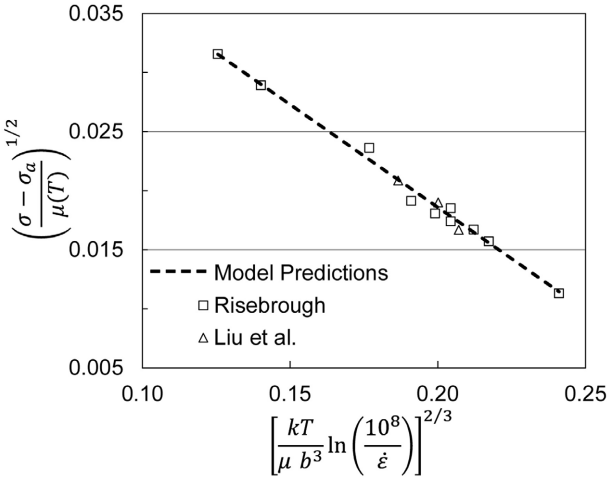

Figure 3. Measurements in pure zinc along with the model fit [2] (F 10.3).

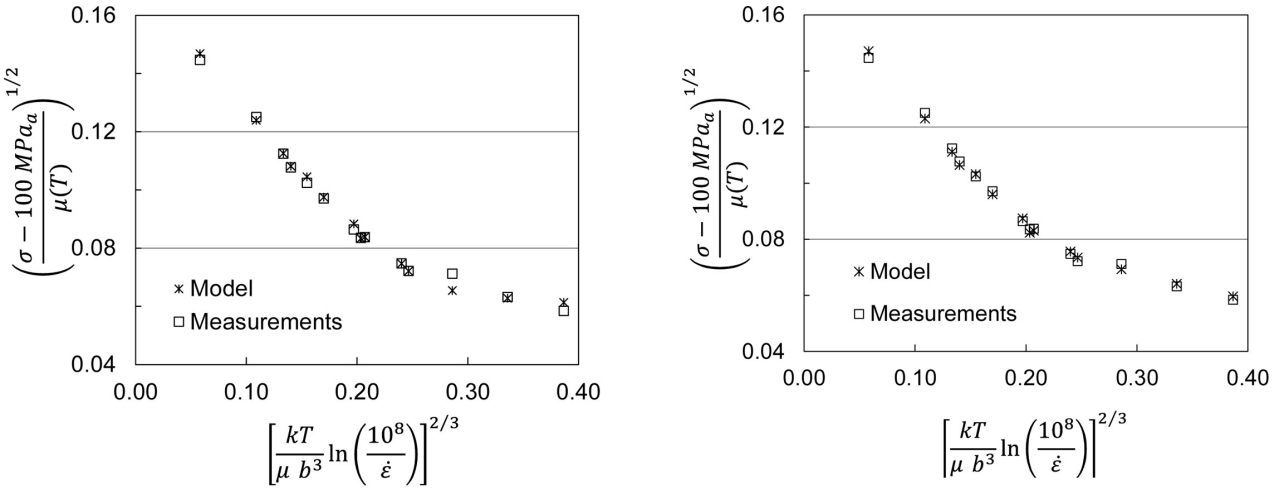

Figure 4. Model fit measurements in the fictitious Follyalloy [2] [5]. (a) Two-obstacle model analysis; (b) Four-obstacle model analysis.

Table 1. Analysis of fictitious folly alloy using a two-obstacle population model and a four-obstacle population model.

	Peierls	Population i_1	Population i_2	Population i_3
$\hat{\sigma}$ (MPa)	2000	400	400	300
g_{oi}	0.15	0.8	0.4	1.6
$\hat{\sigma}$ (MPa)	2500	530		
g_{oi}	0.19	4.2		

is 0.0075 in the two-obstacle analysis and 0.0051 in the four-obstacle analysis. The major difference in the model parameters is in the value of the activation energies. This is an entirely fictitious material and data set, but it demonstrates that assuming two active strengthening mechanisms when having more than two are active can lead to unrealistic values of the model parame-

ters, particularly the activation energies.

In the next section the model parameters assessed for a number of FCC, BCC, and HCP metals are tabulated to enable the observation of trends. In none of these cases is it assumed that more than two strengthening mechanisms are dominant. (This applies to metals in the annealed condition. When strain hardening occurs, the stored dislocation density becomes a third strengthening mechanism, as defined in Equation (3) when $n = 2$). While there are some "high" values of the activation energy reported, there is no case that mirrors the fictitious alloy described in this section.

4. Model Parameters Assessed in Various Metals

4.1. YSA Example in Nominally Pure FCC and HCP Metals

The first class to consider are pure and nominally pure FCC and HCP metals and some simple FCC alloys. These would have at most a single activation energy, which implies a single mechanical threshold stress. Table 2 lists the metals that have been examined. Included is the reference to the raw data, the purity level, the threshold stress normalized by μ_o, the normalized activation energy g_{oi}, and the value of the constant $\dot{\varepsilon}_{oi}$. Note that in 0.9999 pure copper, there is no contribution from impurity elements, *i.e.*, there is no obstacle 1. In the slightly less pure (0.9995) copper used by Dalle Torre *et al.* [12], the impurities introduced an obstacle 1, characterized by $\hat{\sigma}_i/\mu_o = 0.00010$. The same is the case for 0.9997+ pure silver. Note that even in highly pure Cd and Zn, a small impurity obstacle seemed to be present.

The Ni-C alloys analyzed by Follansbee and Gray [7] are characterized by a single value of the normalized activation energy (0.20) but $\hat{\sigma}_i/\mu_o$ values that increase by almost ×10 when the carbon concentration increases from 55 ppm to

Table 2. Model parameters in several FCC and HCP metals analyzed using a single obstacle population model.

Material	Purity	Reference		Obstacle 1		
		Data	Analysis	$\hat{\sigma}_i/\mu_o$	g_{o1}	$\dot{\varepsilon}_{o1}$ (s^{-1})
Cadmium	0.9999	[13]	[2] (T 10.4)	0.0075	0.20	10^7
Zinc	0.99999	[10] [11]	[2] (T 10.2)	0.00285	0.17	10^7
Copper	0.9999	[1]	[1]		None	
Copper	0.9995	[12]	[14]	0.00010	0.6	10^7
Nickel	0.999/55 ppm C	[7]	[7]	0.00034	0.20	10^9
Nickel - C	1900 ppm C	[7]	[7]	0.00300	0.20	10^9
Copper - Al	2000 ppm Al	[2]	[2] (T 8.12)	0.00031	0.6	10^7
Copper - Al	60,000 ppm Al	[2]	[2] (T 8.12)	0.00450	0.6	10^7
Silver	0.9997+	[15]	[16]	0.0020	0.65	10^7
Monel	320,000 ppm Cu	[17]	[17]	0.00224	0.539	10^7
				$p_{\hat{\imath}1} = 0.5$; $q_{\hat{\imath}1} = 1.5$		

1900 ppm. The trends in the Cu-Al alloys are very similar.

It is noteworthy that for all of the materials listed in Table 2 the normalized activation energy is in the range $0.017 \le g_{oi} \le 0.06$. In these metals, the values of p_{i1} and q_{i1} are not allowed to vary and the variation of the value $\dot{\varepsilon}_{oi}$ is of no consequence (since $\dot{\varepsilon} \ll \dot{\varepsilon}_{oi}$).

4.2. YSA Examples in HCP Metals and an Austenitic Stainless Steel

The next class of materials to consider includes several HCP metals and alloys that seem to be strengthened by two operative strengthening mechanisms. In this case Equation (4) applies. Table 3 lists the metals analyzed. The obstacle population referred to as "1" has a very low value of g_{o1}. Obstacle "2", however, is characterized by a g_{o2} value of 1 or higher. It is interesting that the g_{o1} and g_{o2} values of Mg and the Mg alloy AZ31 are identical. Only the value of the $\hat{\sigma}_i/\mu_o$ values changes; the threshold stresses in AZ31 are higher than those in pure Mg. The same is true in pure Ti in the Ti-6Al-4V alloy.

The g_{o2} value in pure Ti and Ti-6Al-4V is 1.6, which seems rather high. The source of this second obstacle population is unclear. Interestingly, an analysis of kinetics in a series of Ti-Al [18] alloys led to the same values of g_{o1} and g_{o2}; alloys with increasing Al contents showed consistently increasing values of $\hat{\sigma}_2/\mu_o$. In fact, the magnitude of the $\hat{\sigma}_2/\mu_o$ term for Ti-6Al-4V is very similar to that predicted by the variation $\hat{\sigma}_2/\mu_o$ from the analysis of the Paton *et al.* measurements. The confusing aspect of this is that the pure Ti analyzed by Doner and Conrad [22] did not have even trace amounts of Al, which suggests the high g_{o2} value in pure Ti does not arise from dislocation interactions with the Al solute. Recall in the hypothetical material considered in Section 3.1 going from a 2-obstacle model to a 4-obstacle model led to more realistic g_o values, as shown in Table 1 and Figure 4(b). Figure 5 shows a similar analysis in pure Ti. In this case, a third obstacle was arbitrarily added. The 3-obstacle model shows slightly better agreement with the measurements, with an error defined by Equation (9) improving from 0.0121 MPa for the 2-obstacle model to 0.0084 MPa for the

Table 3. Model parameters in several FCC and HCP metals analyzed using a two-obstacle population model.

Material	Purity	Reference		Obstacle 1			Obstacle 2		
		Data	Analysis	$\hat{\sigma}_i/\mu_o$	g_{o1}	$\dot{\varepsilon}_{o1}$ (s^{-1})	$\hat{\sigma}_2/\mu_o$	g_{o2}	$\dot{\varepsilon}_{o2}$ (s^{-1})
Zirconium	50 ppm O	[19]	[2] (T 10.12)	0.044	0.15	10^8	0.005	1	10^8
Magnesium	0.9996	[20]	[2] (T 10.5)	0.03	0.35	10^7	0.005	1	10^8
Mg AZ31	3 Al 1 Zn	[21]	[2] (T 10.8)	0.08	0.35	10^7	0.0095	1	10^8
Titanium	5000 ppm O_{eq}/500 ppm Fe	[22] [23]	[2] (T 10.16)	0.0085	0.25	10^7	0.0065	1.6	10^{10}
Ti-6Al-4V		[24]	[21]	0.0185	0.25	10^7	0.0232	1.6	10^{10}
AISI 316 SS	500 ppm N	[25]	[26]	0.0080	0.20	10^8	0.0025	1.7	10^8
				$p_{i1} = 0.5$; $q_{i1} = 1.5$			$p_{i2} = 0.5$; $q_{i2} = 1.5$		

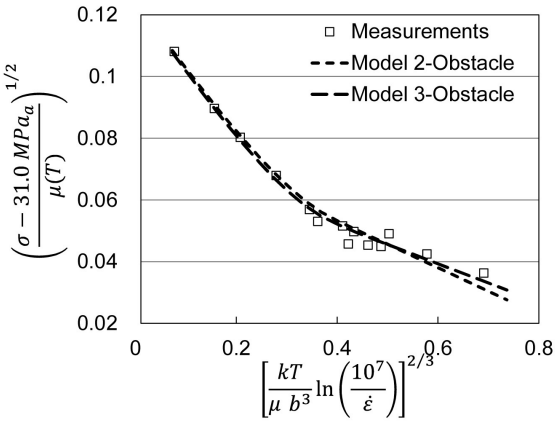

Figure 5. Model fits in pure titanium using a two- and a three-obstacle population model.

3-obstacle model. Table 4 lists the g_o and the $\hat{\sigma}/\mu_o$ values. While somewhat improved agreement between model predictions and measurements going from a 2-obstacle model to a 3-obstacle model, the improvement does not justify the arbitrariness of the model assumption.

A two-obstacle model is required to capture the curvature observed in the plots of yield stress versus temperature and strain rate, as illustrated in Figure 2 and Figure 3. One of the obstacle populations has a low value of the normalized activation energy, with $0.015 \le g_{o1} \le 0.035$ in the metals included in Table 3. These activation energies are similar to those observed in Table 2 in pure FCC metals and FCC alloys, which suggests the obstacles are solute atoms. The second obstacle population is characterized by much higher normalized activation energies, with $1.0 \le g_{o2} \le 1.5$ in the metals included in Table 3. These represent longer-range dislocation-obstacle interactions. It is hard to speculate the active strengthening mechanism. This may reflect solute clusters or precipitates, such as carbides or oxides.

Also included in Table 4 is AISI 316 stainless steel, which is an FCC metal with numerous elemental additions. As indicated in Table 4, a two-obstacle model has been applied. Obstacle 1 has a g_{oi} value characteristic of solution hardening. Indeed, both N and O are effective strengthening solutes in these alloys. Obstacle 2 shows a high value of g_{o2} (1.7). This may reflect the summation of various other solute additions, or it may reflect interaction of dislocations with the various carbides that form in these materials.

4.3. YSA Examples in BCC Metals and Alloys

The next class to consider is pure BCC metals and BCC alloys. Table 5 shows results for six pure BCC metals as well as for AISI 1018 steel. BCC metals are strengthened by the Peierls barrier, which is a short-range obstacle. Indeed, the g_{op} values are in the range $0.07 \le g_{op} \le 0.105$ for this selection of metals. Each of these metals was analyzed using a two-obstacle model [8] and the second obstacle population is assumed to represent dislocation- solute interactions. The g_{o2}

Table 4. Model parameters in pure titanium for the model fits presented in **Figure 5**.

	Two Obstacle Population Analysis		
	Population i_1		Population i_2
$\hat{\sigma}$ (MPa)	405	400	300
g_{oi}	0.25	0.4	1.6
	Error = 0.021 MPa		
	Three Obstacle Population Analysis		
	Population i_1	Population i_2	Population i_3
$\hat{\sigma}$ (MPa)	343	114	281
g_{oi}	0.26	0.34	1.5
	Error = 0.0084 MPa		

Table 5. Model parameters for several pure BCC metals and for AISI 1018 steel using a two-strengthening contribution model.

Material	Purity	Reference		Obstacle 1		Obstacle 2	
		Data	Analysis	$\hat{\sigma}_i/\mu_o$	g_{o1}	$\hat{\sigma}_2/\mu_o$	g_{o2}
Iron	200 ppm C	[27]	[8]	0.0193	0.096	0.0046	0.4
Niobium	0.9984	[9]	[8]	0.032	0.10	0.0057	0.37
Vanadium	0.9986	[28]	[8]	0.013	0.10	0.0020	1.0
Tantalum	0.999	[29]	[8]	0.0145	0.081	0.0048	0.40
Molybdenum	0.9996	[9]	[8]	0.0108	0.07	0.0030	0.27
Tungsten	0.9999	[30] [31]	[8]	0.0017	0.105	0.0036	0.7
AISI 1018 Steel	~0.99; 1800 ppm C	[32]	[2] (T 9.11)	0.014	0.11	0.0050	1.0
				$p_{i1} = p_{i2} = 0.5$; $q_{i1} = q_{i2} = 1.5$			
				$\dot{\varepsilon}_{o1} = 10^8\ s^{-1}$		$\dot{\varepsilon}_{o2} = 10^{10}\ s^{-1}$	

values in **Table 5** are consistent with this; they fall in the range $0.27 \le g_{o2} \le 1.0$. The associated values for vanadium and 1018 steel are $g_{o2} = 1.0$ which is on the high side. The source of this high value in vanadium is unclear. In 1018 steel, this value may represent the combined contributions of several of the solute additions in this metal, as demonstrated in Section 3.1. Certainly, as indicated by the values of $\hat{\sigma}_p/\mu_o$, this strengthening contribution decreases strongly with increasing temperature and decreasing strain rate. Dislocation-solute atom interactions essentially define strengthening at high temperatures and low strain rates. In Section 3, it was mentioned that the strengthening contribution of the Peierls barrier in molybdenum goes to zero at just over 500 K (at a strain rate of 0.001 s^{-1}). Yet, this metal exhibits considerable yield stresses all the way to 1000 K at this strain rate.

5. YSA Observations of Concentration Dependence in Several Metals

In several of the systems studied, a range of compositions of one of the main solute additions has enabled an assessment of the variation of the threshold stress with composition. This was possible in Fe-C [8], Ni-C [7], Fe-Al [2], Zirconium [2], and Ti-Al [26]. In addition, experimental studies have been performed to analyze the effect of N additions in 316 L stainless steel [33]. **Figure 6** shows a compilation of the results. Plotted is $\hat{\sigma}_i/\mu_o$ versus composition for these five alloys. Several theories and experimental studies suggest that the strength increase due to solution hardening should vary as the square-root of the composition [34]. The strengthening contributions in **Figure 6** are plotted versus composition to the power of one. The limited data available support a linear model. The dashed lines in **Figure 6** start close to zero at a zero concentration and show increased hardening with an increasing concentration. Carbon in Fe and Al in Ti appear to be quite effective strengtheners. Carbon in nickel and nitrogen in 316 SS are less effective strengtheners. Aluminum in Cu also is an effective strengthener. The effect of model assumptions on these observations should be considered. In Ni-C and Cu-Al, a one-obstacle model has been applied. In the other metals plotted in **Figure 6**, a two-obstacle model has been applied. If in fact, one or more additional solute elements contribute to strengthening (*i.e.*, the $\hat{\sigma}_i$ term), then the effects of all of these combine to set the value of $\hat{\sigma}_i$. If this were the case in Fe-C, then $\hat{\sigma}_i$ has been over-estimated. Evidence in opposition to this possibility is that at concentrations approaching zero, the strengthening contributions all start close to zero. If another solute were contributing to strengthening one would expect an intercept at a positive value on the ordinate. While for Fe-C, Ti-Al, and 316 SS-N, the intercepts are all positive in **Figure 6**, they are at relatively low values of $\hat{\sigma}_i/\mu_o$, and plotting the strength contributions versus the square-root of the concentration would take the intercepts even closer to zero. Nonetheless, the importance of this model assumption needs to be

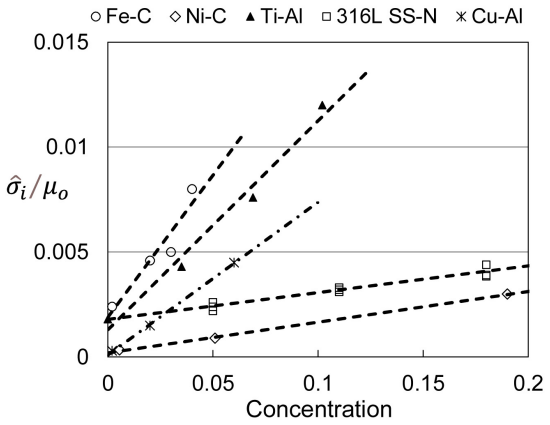

Figure 6. Variation of the threshold stress characterizing solute atom interactions with concentration in several alloys.

considered when evaluating solute strengthening in alloys using the MTS methodology.

6. Compilation of Observations in Strain Hardening (EA)

Equation (4) and Equation (5) identified the governing equations for strain hardening, which is also referred to as "structural evolution". The ensuing analysis of evolution was referred to earlier as the "Evolution" Kinetic Analysis (EA). Key to the application of these equations is the variation of $\hat{\sigma}_\varepsilon$ with strain for stress-strain curves at various temperatures and strain rates. The most rigorous way to compute the variation of $\hat{\sigma}_\varepsilon$ with strain is to estimate $\hat{\sigma}_\varepsilon$ using samples prestrained at a specified temperature and strain rate to a specified strain, and then reloaded at various temperatures and strain rates. These experiments give the variation of yield stress on these prestrained samples with temperature and strain rate. Fitting this data set to Equation (3) gives the value of $\hat{\sigma}_\varepsilon$. Repeating this pretraining operation at the same temperature and strain rate but to different strain levels enables one to estimate the $\hat{\sigma}_\varepsilon$ versus strain curve, which can be fit to Equation (4) to give values of q_{II} and $\hat{\sigma}_{\varepsilon s}$ for that prestrain temperature and strain rate. This test sequence must be repeated at various prestrain temperatures and strain rates to give these model parameters (θ_{II} and $\hat{\sigma}_{\varepsilon s}$) at these temperatures and strain rates. While this rigorous test sequence necessitates a great number of stress versus strain measurements, this is precisely the approach used in copper [1], nickel and several Ni-C alloys [7], and Ti-6Al-4V [24].

Figure 7(a) shows the compilation of measurements in Oxygen Free Electronic Copper [1]. The solid lines are drawn according to Equation (4) with $\kappa = 2$. As described above each value of $\hat{\sigma}_\varepsilon$ plotted in **Figure 7(a)** represents the analysis of yield stress measurements at various temperatures and strain rates plotted according to Equation (3). The availability of this massive data set

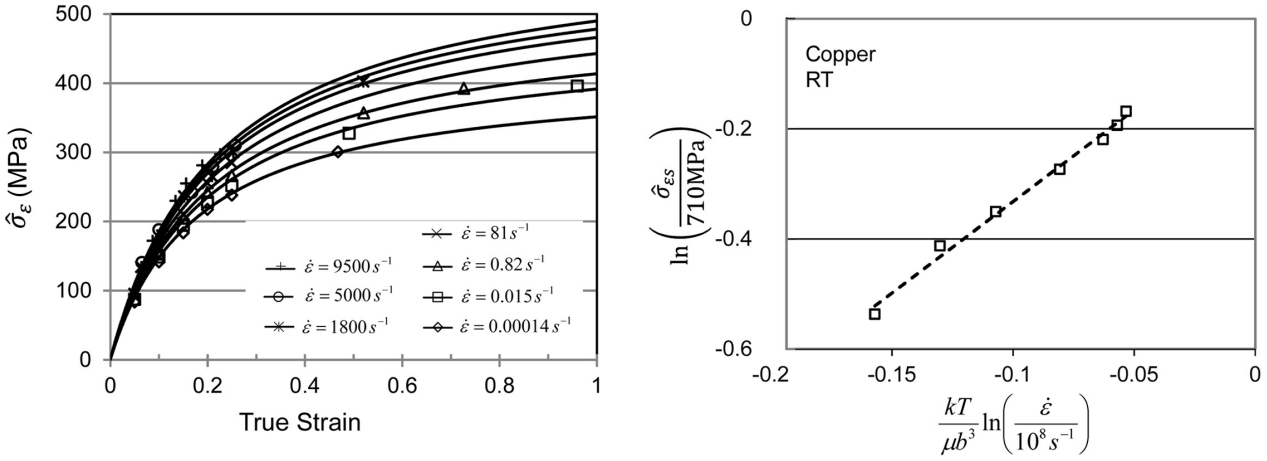

Figure 7. Variation of the threshold stress characterizing dislocation interactions with the stored dislocation density as a function of strain rate. (a) Measurements in pure copper [2] (F 8.2); (b) Fit of the saturation threshold stress with temperature strain rate according to Equation (5) [2] (F 8.3).

enabled the optimal selection of model variables in this equation [2]. The selected model variables were $p_\varepsilon = 2/3$, $q_\varepsilon = 1$, $g_{o\varepsilon} = 1.6$, and $\dot{\varepsilon}_{oe} = 10^7\ s^{-1}$. These values were found to work equally well in nickel [7] and Ti-6Al-4V [24]. Accordingly, these values have been used for all metals and alloys; they are not treated as variables. Similarly, the measurements in Ni-C [7] led to the selection of s_i parameters in Equation (2) for the solution hardening obstacle population. In this case, as shown in **Table 2**, $p_i = 0.5$, $q_i = 1.5$, and $\dot{\varepsilon}_{oi} = 10^9\ s^{-1}$. These values have been used for many solution-hardened metals and alloys.

It is evident that as the strain rate increases the curves in **Figure 7(a)** trend toward higher saturation stresses—$\hat{\sigma}_{\varepsilon s}$. **Figure 7(b)** shows the plot of saturation stress versus strain rate according to Equation (5). A value of $\hat{\sigma}_{\varepsilon so}$ equal to 710 MPa forces the dashed line through the origin, as specified by Equation (5).

A less rigorous procedure for estimating the variation of $\hat{\sigma}_\varepsilon$ with strain is to solve Equation (3) for $\hat{\sigma}_\varepsilon$ directly from the stress-strain curve. The operating equation for a metal with two obstacle populations (e.g., a BCC metal with a Peierls stress and an impurity atom stress) becomes

$$\hat{\sigma}_\varepsilon = \frac{\mu_o}{s_\varepsilon(\dot{\varepsilon},T)}\left[\frac{\sigma}{\mu} - \frac{\sigma_a}{\mu} - s_p(\dot{\varepsilon},T)\frac{\hat{\sigma}_p}{\mu_o} - s_i(\dot{\varepsilon},T)\frac{\hat{\sigma}_i}{\mu_o}\right]. \tag{10}$$

This is the approach taken in evaluating strain hardening in austenitic stainless steels [35], Inconel 718 [36], and several other of the metals and alloys described by Follansbee [2]. **Figure 8** gives an example of this procedure for measurements in Inconel 718 reported by Nalawade *et al.* [37] at two test temperatures. Measurements at several test temperatures and strain rates enable one to evaluate Equation (5) and solve for $\hat{\sigma}_{\varepsilon so}$ and $g_{\varepsilon so}$. Application of Equation (4) to the curves in **Figure 7(a)** and **Figure 8** also gives values of the stage II hardening rate θ_{II}. This has been observed to have a slight strain rate dependence but no measurable temperature dependence given by

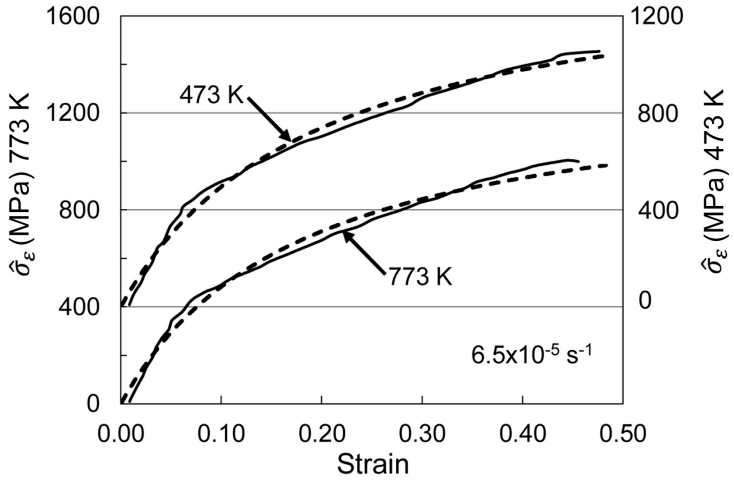

Figure 8. Deduced variation of the threshold stress characterizing dislocation interactions with the stored dislocation density in Inconel 718 at two test temperatures [2] (F 12.11).

$$\theta_{II} = A_o + A_1 \ln \dot{\varepsilon} + A_2 \sqrt{\dot{\varepsilon}} \tag{11}$$

where A_o, A_1, and A_2 are constants.

In the next sections, assessed values of $\hat{\sigma}_{\varepsilon so}$, $g_{\varepsilon so}$, and θ_{II} (actually A_o) are reviewed for several pure metals and alloys. The results are presented in tabular form. Included are references to the original data source and references to the publications that detail the data analyses.

6.1. EA Observations in Several FCC and HCP Metals

Table 6 lists values of $\hat{\sigma}_{\varepsilon so}/\mu_o$, $g_{\varepsilon so}$, and θ_{II}/μ_o (Equation (4) and Equation (5)) for several pure FCC and HCP metals and several FCC alloys. Also included are the values of κ and $\dot{\varepsilon}_{\varepsilon so}$ used in the analyses and reference to the raw data and source for the analysis. The values of θ_{II}/μ_o (actually, listed in Table 6 is A_o from Equation (11), but this is only slightly less than θ_{II}) fall generally in the range $A_o/\mu_o = 0.04 \pm 0.01$. Kocks and Mecking [38] observed that $\hat{\sigma}_{\varepsilon so}/\mu_o$ correlated with the stacking fault energy γ_{SF} in Cu, Al, Ni and Ag. Table 7 lists the values of these parameters reported by Kocks and Mecking along with additional values reported Cu, Ni, Ag, and other FCC alloys; these values tend to fall directly in line with the Kocks and Mecking values. Figure 9 gives the updated plot of $\hat{\sigma}_{\varepsilon so}/\mu_o$ versus γ_{SF}. The alloys tend to have lower values of γ_{SF}, which is consistent with a model proposed by Lee *et al.* [39]. The correlation shown in Figure 9 is a very interesting result that allows for predictions of $\hat{\sigma}_{\varepsilon so}/\mu_o$ for an unknown FCC metal or alloy, given that γ_{SF} is known. Of course, measurements of γ_{SF} can be quite variable and open to interpretation. An excellent review of these measurements along with estimates of the most "likely" values for several FCC systems was published by Gallagher [40][2].

Table 6. Model parameters characterizing structure evolution in several HCP and FCC metals.

Material	Reference		κ	$\hat{\sigma}_{\varepsilon so}/\mu_o$	$\dot{\varepsilon}_{\varepsilon so}$ (s^{-1})	$g_{\varepsilon so}$	θ_{II}/μ_o [a]
	Data	Analysis					
Cadmium	[10]	[2] (T 10.4)	1	0.00578	10^7	0.0819	0.0404
Zinc	[10] [11]	[2] (T 10.2)	1	0.0224	10^7	0.0335	0.0272
Copper	[1]	[2] (T 8.4)	2	0.0155	10^8	0.301	0.0522
Nickel	[7]	[2] (T 8.9)	2	0.0148	10^8	0.168	0.0541
Nickel-1900C	[7]	[7]	2	0.0151	10^8	1.171	0.0541
Copper-0.2Al	[2]	[2] (F 8.45)[b]	2	0.0188	10^8	0.282	0.0546
Copper-6Al	[2]	[2] (F 8.45)	2	0.0732	10^8	0.247	0.0546
Silver	[14]	[16]	2	0.0245	10^8	0.285	0.0514
Monel	[17]	[19]	[c]	0.0080	10^8	0.37	0.0395

[a]The numerator is actually A_0 in Equation (11). [b]There is an error in the caption of Figure 8.45 in [2]. The value listed in Table 8.13 are the values at 295 K and 0.0015 s^{-1}; the 0 K values are listed in this table. [c]Gray *et al.* [17] use another form of Equation (4) for the differential hardening behavior.

[2]The recommended γ_{SF} values reported by Gallagher for Cu, Ni, and Ag are the values included in Table 7.

Table 7. Saturation threshold stress and stacking fault energy in several FCC metals.

Material	Reference	$\hat{\sigma}_{\varepsilon so}$	μ_o	b	γ_{SF}	$\gamma_{SF}/\mu_o b$
		MPa	MPa	nm	ergs/cm^2	
Cu	[2] (T 8.4)	710	45,780	0.256	55	0.00469
Cu-2Al	[2] (F 8.45)	975	45,780	0.256	25	0.00213
Cu-6Al	[2] (F 8.45)	3350	45,780	0.256	6	0.00051
Ni	[2] (T 8.9)	1180	85,090	0.249	250	0.01180
Ag	[14]	761	3110	0.289	22	0.00245
AISI 316 SS	[2] (T 11.6)	2600	71,460	0.249	22	0.00169
Al	[38][a]	304	28,820	0.286	190	0.02305
Ni		897	85,090	0.249	275	0.01298
Cu		783	45,780	0.256	56	0.00476
Ag		817	31,100	0.289	16	0.00178

[a]Kocks and Mecking reported $\gamma_{SF}/\mu_o b$. γ_{SF} values are computed using μ_o and b.

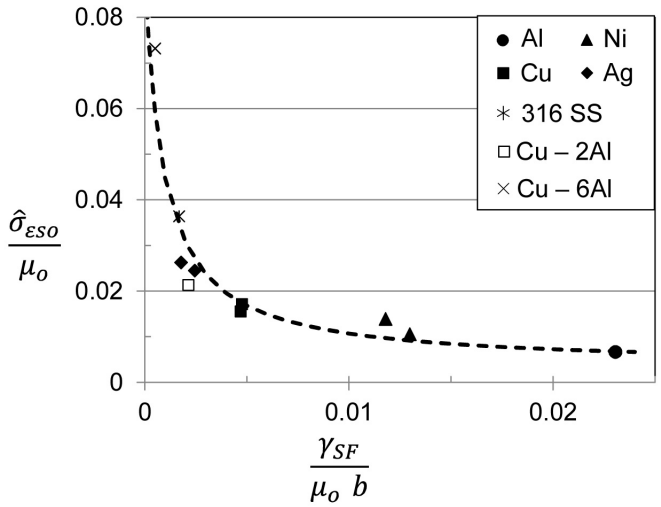

Figure 9. Variation of the saturation threshold stress with stacking fault energy for the FCC met listed in Table versus stacking fault energy shear FCC metals listed in **Table 7**.

6.2. EA Observations in BCC Metal

Table 8 lists values of $\hat{\sigma}_{\varepsilon so}/\mu_o$, $g_{\varepsilon so}$, and A_o/μ_o for several pure BCC metals and AISI 1018 steel. Included in this table are the values of κ and $\dot{\varepsilon}_{\varepsilon so}$ used in the analyses and reference to the raw data and source for the analysis. The values of $\hat{\sigma}_{\varepsilon so}/\mu_o$ and $g_{\varepsilon so}$ are somewhat dependent upon the value of κ used in the analysis. For example, in vanadium when κ is selected as 2 instead of 3, $\hat{\sigma}_{\varepsilon so}/\mu_o$ decreases from 0.00896 to 0.00605 and $g_{\varepsilon so}$ increases from 0.233 to 0.377. The rows for molybdenum show some variability in the EA values according to the κ variable selected as well as the estimate of the strain introduced by prior warm work in the material—ε_{ww} [5].

Table 8. Saturation threshold stress and stacking fault energy in several BCC metals. The estimates in molybdenum vary with details of the analysis.

Material	Reference	$\hat{\sigma}_{\varepsilon so}/\mu_o$	$\dot{\varepsilon}_{\varepsilon so}$ (s^{-1})	$g_{\varepsilon so}$	θ_{II}/μ_o [a]	κ
Niobium	[2] (T 9.17)	0.0125	10^8	0.219	0.0252	2
1018 Steel	[2] (T 9.11)	0.00904	10^{10}	0.468	0.0476	2
Vanadium	[2] (T 9.13)	0.00896	10^{10}	0.233	0.0518	3
Vanadium		0.00605	10^{10}	0.377	0.0518	2
Tungsten	[2] (T 14.4)	0.00468	10^8	0.0748	0.0202	2
Tantalum	[41][b]	0.00653	10^8	0.242	0.00507	2
Molybdenum $\varepsilon_{ww} = 0.2$	[5]	0.0112	10^8	0.136	0.0105	1
Molybdenum $\varepsilon_{ww} = 0.2$	[5]	0.0111	10^8	0.206	0.0135	2
Molybdenum $\varepsilon_{ww} = 0.1$	[5]	0.0075	10^8	0.200	0.0144	1

[a]The numerator is actually A_0 in Equation (11). [b]The cited reference gives the source of the data; the analysis was performed in creating this manuscript. The former is also the case with the analysis of vanadium for $\kappa = 2$.

The values of A_0/μ_o fall generally in the range $A_0/\mu_o = 0.032 \pm 0.018$. This is slightly below the values seen in the FCC metals, and there is more variability than seen in the FCC metals. This observation may simply reflect the general uncertainty in these measurements. The values of $\hat{\sigma}_{\varepsilon so}/\mu_o$ do not exhibit a clear trend with any physical property. **Figure 10** plots $\hat{\sigma}_{\varepsilon so}$ versus the shear modulus μ_o. Error bars are shown for the vanadium and molybdenum estimates. One could argue that the saturation threshold stress increases with increasing modulus, but the confidence in this trend is not high.

7. Discussion

This manuscript has outlined application of the MTS constitutive model in several FCC, BCC, and HCP metals. Section 1 and Section 2 provided an overview of the operative equations. Included in Section 2 was a discussion of how to apply Equation (1) and select a value of n for an alloy with multiple alloying additions. The rationale for linearly adding the individual strengthening contributions was also briefly considered. A critically important feature of the MTS methodology is the distinction of the kinetics affecting the yield stress (where the yield stress implies yield following any processing history) evaluated using the Yield Stress Kinetics Analysis (YSA), from the kinetics affecting strain hardening, or structure evolution, evaluated using the Evolution Kinetics Analysis (EA). A constitutive formalism that does not provide this distinction, e.g., the Johnson

Cook constitutive model [42] or the Armstrong Zerilli constitutive model [43] can replicate stress levels under constant strain rate and temperature conditions, but will be unable to accurately describe instantaneous path changes, e.g., strain rate or temperature changes. This, in turn, will affect predictions of instabilities, e.g., necking in a tensile test or shear band initiation.

Section 3 through Section 5 reviewed results of the YSA model application for several FCC, HCP, and BCC metals and alloys. For some FCC and HCP metals, the yield stress measurements can be modeled using a single obstacle population (**Table 2**). Application of the model to several other FCC and HCP metals necessitates a two-obstacle population model (**Table 3**). All of the BCC metals analyzed required a two-obstacle population model (**Table 5**). Common trends for the normalized activation energies across all metals and alloys were identified. Based on these observations, it is concluded that the yield stress kinetic analysis is a fairly descriptive constitutive formalism.

Section 6 reviewed experience with application with structure evolution using the EA equations. For FCC metals, there exists a clear variation of $\hat{\sigma}_{\varepsilon so}$ with-stacking fault energy (**Table 7** and **Figure 9**). No trends with $g_{\varepsilon so}$ were noted. For BCC metals, a weak correlation between $\hat{\sigma}_{\varepsilon so}$ and the shear modulus was illustrated in **Figure 10**. For all metals analyzed, the stage II hardening rate (actually, A_o in Equation (11)), consistently was in the range $A_o/\mu_o = 0.037 \pm 0.018$. This translates to $A_0 \approx \mu_o/27$. Kocks and Mecking [38] report that the Stage II hardening rate is in the range $\theta_{II} \approx \mu_o/115$, which is 4x less than the estimate here. This difference may reflect the common practice of evaluating Equation (4) to large-strain behavior rather than near-yield behavior.

The largest problem with the structure evolution analysis, particularly with BCC and some HCP metals, however, is in the generality of Equation (4). This equation was based on the Voce equation [44][3]. The Voce equation models the

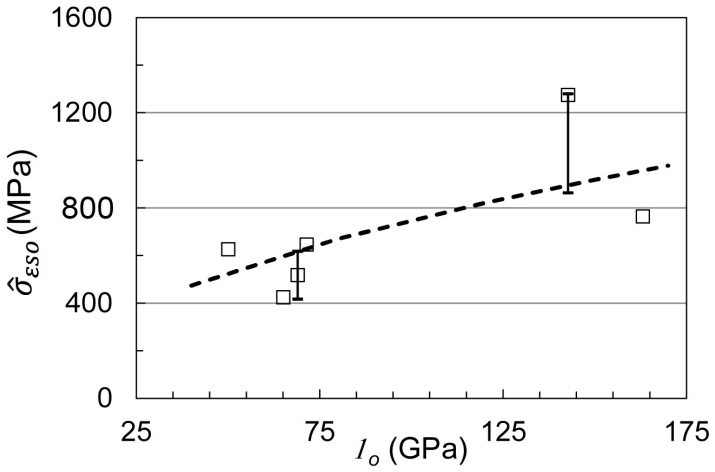

Figure 10. Variation of the saturation threshold stress versus shear modulus in the BCC metals listed in **Table 8**.

[3]When $\kappa = 1$ Equation (4) becomes the Voce equation.

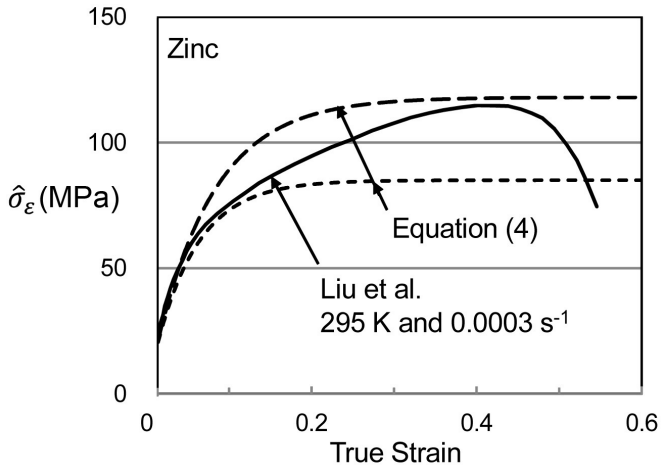

Figure 11. Variation of the saturation threshold stress characterizing zinc where deformation twinning may be active.

balance between dislocation generation and recovery in strain hardening. Estrin [45] has derived the Voce equation based on dislocation density contributions. The Voce equation—or the slightly modified version with κ equal to 2 in Equation (4)—provides an adequate fit to the evolution of $\hat{\sigma}_\varepsilon$ with strain in Cu and Ni and many other metals (e.g., **Figure 7(a)** and **Figure 8**). The Voce equation breaks down, however, when strain hardening is accompanied by deformation twinning, dynamic strain aging, or stress or strain induced metallurgical transformations. The effects of deformation twinning were observed in zirconium [2], zinc, and several other materials. **Figure 11** shows that the variation of $\hat{\sigma}_\varepsilon$ with strain in 0.99999 Zn with a grain size of 70 μm [11] is not well-described using Equation (4) [2]. It is suspected that deformation twinning is effectively decreasing the grain size and leading to an increasing contribution from dislocation interactions with grain boundaries (e.g., the σ_a variable in Equation (1)) [2]. Dynamic strain aging was observed to be prevalent in niobium, titanium, austenitic stainless steels, and nickel based superalloys [46]. Signatures of the contributions of these metallurgical processes in context of the application of the MTS formalism were noted [46].

The conclusion is that large deviations from evolution predicted by Equation (4) are possible in many metals and alloys. The Evolution Kinetics Analysis that comprises the MTS model is not as widely applicable across myriad metals and alloys as is the Yield Stress Kinetics Analysis. This conclusion may guide further research and modeling of strain hardening, particularly when dislocation storage is accompanied by deformation twinning, dynamic strain aging, or stress or strain induced phase transformations.

Acknowledgements

Much of this research was supported by Saint Vincent College. The author acknowledges the collaboration with U. F. (Fred) Kocks, who recently passed away. Fred was a colleague and friend who mentored me on topics related to deforma-

tion kinetics. The world has lost one of the top materials scientists of the 20th century.

Conflicts of Interest

The author declares no conflicts of interest regarding the publication of this paper.

References

[1] Follansbee, P.S. and Kocks, U.F. (1988) A Constitutive Description of the Deformation of Copper Based on the Use of the Mechanical Threshold Stress as an Internal State Variable. *Acta Metallurgica*, **36**, 81-93. https://doi.org/10.1016/0001-6160(88)90030-2

[2] Follansbee, P.S. (2022) Fundamentals of Strength: Principles, Experiment, and Applications of an Internal State Variable Constitutive Formulation. 2nd Edition, Springer Nature, Cham. https://doi.org/10.1007/978-3-031-04556-1

[3] Follansbee, P.S. (2014) On the Definition of State Variables for an Internal State Variable Constitutive Model Describing Metal Deformation. *Materials Sciences and Applications*, **5**. https://doi.org/10.4236/msa.2014.58062

[4] Kocks, U.F., Argon, A.S. and Ashby, M.F. (1975) Thermodynamics and Kinetics of Slip. In: Chalmers, B., Christian, J.W. and Massalski, T.B., Eds., *Progress in Materials Science*, Pergamon Press, Oxford, 4.

[5] Follansbee, P.S. (2022) MTS Model Application to Materials Not Starting in the Annealed Condition. *Materials*, **15**, Article 7874. https://doi.org/10.3390/ma15227874

[6] Kocks, U.F. (1976) Laws for Work Hardening and Low Temperature Creep. *Journal of Engineering Materials Technology*, **98**, 76-85. https://doi.org/10.1115/1.3443340

[7] Follansbee, P.S., Huang, J.C. and Gray, G.T. (1990) Low-Temperature and High-Strain-Rate Deformation of Nickel and Nickel-Carbon Alloys and Analysis of the Constitutive Behavior According to an Internal State Variable Model. *Acta Metallurgica et Materialia*, **38**, 1241-1254. https://doi.org/10.1016/0956-7151(90)90195-M

[8] Follansbee, P.S. (2010) Analysis of Deformation Kinetics in Seven Body-Centered Cubic Pure Metals Using a Two-Obstacle Model. *Metallurgical and Materials Transactions A*, **41**, 3080-3090. https://doi.org/10.1007/s11661-010-0372-6

[9] Briggs, T.L. and Campbell, J.D. (1972) The Effect of Strain Rate and Temperature on the Yield and Flow of Polycrystalline Niobium and Molybdenum. *Acta Metallurgica*, **20**, 711-724. https://doi.org/10.1016/0001-6160(72)90100-9

[10] Risebrough, N.R. (1965) The Deformation Characteristic of Zinc and Cadmium. Ph.D. Thesis, University of British Columbia, Vancouver.

[11] Liu, H., Huang, C.X., Wu, S.D. and Zhang, Z.F. (2008) Tensile Deformation and Fracture Behaviors of High Purity Polycrystalline Zinc. *Materials Science and Engineering: A*, **490**, 117-125. https://doi.org/10.1016/j.msea.2008.01.004

[12] Dalla Torre, F.H., Pereloma, E.V. and Davies, C.H.J. (2006) Strain Hardening Behaviour and Deformation Kinetics of Cu Deformed by Equal Channel Angular Extrusion from 1 to 16 Passes. *Acta Materialia*, **54**, 1135-1146. https://doi.org/10.1016/j.actamat.2005.10.041

[13] Mannan, S.L. and Rodriguez, P. (1975) Grain Size Dependence of the Deformation

Behaviour of Cadmium. *Acta Metallurgica*, **23**, 221-228. https://doi.org/10.1016/0001-6160(75)90187-X

[14] Follansbee, P.S. (2022) Application of the Mechanical Threshold Stress Model to Large Strain Processing. *Materials Sciences and Applications*, **13**, 300-316. https://doi.org/10.4236/msa.2022.135016

[15] Carreker Jr., R.P. (1957) Tensile Deformation in Silver as a Function of Temperature, Strain Rate, and Grain Size. *JOM*, **9**, 112-115. https://doi.org/10.1007/BF03398466

[16] Malone, S. (2019) Deformation Twinning in Silver. Senior Capstone Project, Saint Vincent College, Latrobe, Pennsylvania, USA.

[17] Gray III, G.T., Chen, S.R. and Vecchio, K.S. (1999) Influence of Grain Size on the Constitutive Response and Substructure Evolution of Monel 400. *Metallurgical and Materials Transactions A*, **30**, 1235-1247. https://doi.org/10.1007/s11661-999-0273-8

[18] Paton, N.E., Williams, J.C. and Rauscher, G.P. (1973) The Deformation of α-Phase Titanium. In: Jaffee, R.I. and Burte, H.M., Eds., *Titanium Science and Technology*, Plenum Press, New York, 1049-1069.

[19] Chen, S.R. and Gray, G.T. (1997) Influence of Twinning on the Constitutive Response of Zr: Experiments and Modeling. 5*th International Conference on Mechanical and Physical Behaviour of Materials under Dynamic Loading*, Toledo, 22-26 September 1997, C3:741-C3:746. https://doi.org/10.1051/jp4:19973126

[20] Suzuki, H., Hashizume, S., Yabuki, Y., Ichihara, Y., Nakajima, S. and Kenimochi, K. (1968) Studies on the Flow Stress of Metals and Alloys. Report of the Institute of Industrial Science, the University of Tokyo.

[21] Takuda, H., Morishita, T., Kinoshita, T. and Shirakawa, N. (2005) Modelling of Formula for Flow Stress of a Magnesium Alloy AZ31 Sheet at Elevated Temperatures. *Journal of Materials Processing Technology*, **164-165**, 1258-1262.

[22] Yin, C.A., Doner, M. and Conrad, H. (1983) Deformation Kinetics of Commercial Ti-50A (0.5 at. Pct Oeq) at Low Temperatures ($T < 0.3\ T_m$). *Metallurgical Transactions A*, **14**, 2545-2556. https://doi.org/10.1007/BF02668896

[23] Doner, M. and Conrad, H. (1973) Deformation Mechanisms in Commercial Ti (0.5 at. Pct Oineq) at Intermediate and High Temperatures (0.3-0.6 tinm). *Metallurgical Transactions*, **4**, 2809-2817. https://doi.org/10.1007/BF02644581

[24] Follansbee, P.S. and Gray, G.T. (1989) An Analysis of the Low Temperature and Low and High Strain Rate Deformation of Ti-6Al-4V. *Metallurgical Transactions A*, **20**, 863-874. https://doi.org/10.1007/BF02651653

[25] Conway, J.B., Stentz, R.H. and Berling, J.T. (1974) Fatigue, Tensile and Relaxation Behavior of Stainless Steels. Report Commissioned by the U.S. Atomic Energy Commission Division of Reactor Research and Development. https://doi.org/10.2172/4239699

[26] Follansbee, P.S. (2012) An Internal State Variable Constitutive Model for Deformation of Austenitic Stainless Steel. *Journal of Engineering Materials and Technology*, **134**, 041007. https://doi.org/10.1115/1.4006822

[27] Nojima, T. (1988) Constitutive Equation of Some Kinds of Steels at High Rates of Strain. In: Chiem, C.Y., Kunze, H.D. and Meyer, L.W., Eds., *Impact Loading and Dynamic Behaviour of Materials*, DGM Informationsgesellschaft Verlag, Bremen, 357-364.

[28] Nemat-Nasser, S. and Guo, W.G. (2000) High Strain-Rate Response of Commer-

cially Pure Vanadium. *Mechanics of Materials*, **32**, 243-260. https://doi.org/10.1016/S0167-6636(99)00056-3

[29] Hoge, K.G, and Mukherjee, A.K. (1977) The Temperature Dependence and Strain Rate Dependence of the Flow Stress of Tantalum. *Journal of Materials Science*, **12**, 1666-1672. https://doi.org/10.1007/BF00542818

[30] Gröger, R. and Vitek, V. (2008) Multiscale Modeling of Plastic Deformation of Molybdenum and Tungsten. III. Effects of Temperature and Plastic Strain Rat. *Acta Materialia*, **56**, 5426-5439. https://doi.org/10.1016/j.actamat.2008.07.027

[31] Brunner, D. and Glebovsky, V. (2000) Analysis of Flow-Stress Measurements of High-Purity Tungsten Single Crystals. *Materials Letters*, **44**, 144-152. https://doi.org/10.1016/S0167-577X(00)00017-3

[32] Gray, G.T. and Chen, S.R. (2007) MST-8 Constitutive Properties & Constitutive Modeling. Los Alamos National Laboratory, LA-CP-07-1590.

[33] Norström, L.Å. (1977) The Influence of Nitrogen and Grain Size on Yield Strength in Type AISI 316L Austenitic Stainless Steel. *Metal Science*, **11**, 208-212. https://doi.org/10.1179/msc.1977.11.6.208

[34] Fleischer, R.L. (1963) Substitutional Solution Hardening. Durcissement de solution par substitution Verfestigung in substitutionsmischkkistallen. *Acta Metallurgica*, **11**, 203-209. https://doi.org/10.1016/0001-6160(63)90213-X

[35] Follansbee, P.S. (2015) Structure Evolution in Austenitic Stainless Steels—A State Variable Model Assessment. *Materials Sciences and Applications*, **6**, 457-463. https://doi.org/10.4236/msa.2015.66049

[36] Follansbee, P.S. (2016) Analysis of Deformation in Inconel 718 When the Stress Anomaly and Dynamic Strain Aging Coexist. *Metallurgical and Materials Transactions A*, **47**, 4455-4466. https://doi.org/10.1007/s11661-016-3609-1

[37] Nalawade, S.A., Sundararaman, M., Kishore, R. and Shah, J.G. (2008) The Influence of Aging on the Serrated Yielding Phenomena in a Nickel-Base Superalloy. *Scripta Materialia*, **59**, 991-994. https://doi.org/10.1016/j.scriptamat.2008.07.004

[38] Kocks, U.F. and Mecking, H. (2003) Physics and Phenomenology of Strain Hardening: The FCC Case. *Progress in Materials Science*, **48**, 171-273. https://doi.org/10.1016/S0079-6425(02)00003-8

[39] Lee, J.Y., Yang, M.K., Song, L., Vitos, L. and Kwon, S.K. (2017) The Behaviour of Stacking Fault Energy upon Interstitial Alloying. *Scientific Reports*, **7**, Article No. 11074. http://www.nature.com/scientificreports https://doi.org/10.1038/s41598-017-11328-4

[40] Gallagher, P.C.J. (1970) The Influence of Alloying, Temperature, and Related Effects on the Stacking Fault Energy. *Metallurgical Transactions*, **1**, 2429-2461. https://doi.org/10.1007/BF03038370

[41] Chen, S.R. and Gray, G.T. (1996) Constitutive Behavior of Tantalum and Tantalum-Tungsten Alloys. *Metallurgical and Materials Transactions A*, **27**, 2994-3006. https://doi.org/10.1007/BF02663849

[42] Johnson, G.R. and Cook, W.H. (1983) A Constitutive Model and Data for Metals Subjected to Large Strains, High Strain Rates, and High Temperatures. *Proceedings 7th International Symposium on Ballistics*, The Hague, 19-21 April 1983, 541-547.

[43] Zerilli, F.J. and Armstrong, R.W. (1987) Dislocation-Mechanics-Based Constitutive Relations for Material Dynamics Calculations. *Journal of Applied Physics*, **61**, 1816-1825. https://doi.org/10.1063/1.338024

[44] Voce, E. (1948) The Relationship between Stress and Strain for Homogeneous De-

formation. *Journal of the Institute of Metals*, **74**, 537-562.

[45] Estrin, Y. (1996) Dislocation-Density-Related Constitutive Modeling. In: Krausz, A.S. and Krausz, K., Eds., *Unified Constitutive Laws for Plastic Deformation*, Academic Press Inc., San Diego, 69-106. https://doi.org/10.1016/B978-012425970-6/50003-5

[46] Follansbee, P.S. (2020) Further Analysis of Dynamic Strain Aging in Context of an Internal State Variable Constitutive Formalism. *Metallurgical and Materials Transactions A*, **51**, 1275-1285. https://doi.org/10.1007/s11661-019-05591-5

Appendix—On the Number of Independent Variables

The number of independent variables in a constitutive equation is an important consideration. The objective is to derive equations with physical significance but with the fewest independent variables. A common objection to a proposed set of constitutive equations is that, with a great many independent variables, it is "easy" to fit the model to a given data set. This Appendix will assess this number for the MTS formalism.

For a metal that can be evaluated using a two-obstacle, $\hat{\sigma}_1$ and $\hat{\sigma}_2$, plus an evolution obstacle, $\hat{\sigma}_\varepsilon$, Equation (3) with $n = 2$ and Equation (2) for each of the (3) s_i values is the governing equation for YSA. Equation (4) and Equation (5) are the governing equations for EA. Table A1 lists the parameters in these equations. Some of the parameters are physical constants. Some are identified as "Independent Variables". For a two-obstacle model, each threshold stress and the values of g_{o1} *and* g_{o2} are listed as independent variables. The corresponding value of $g_{o\varepsilon}$ is listed as a "Constrained Variable", since as outlined in the discussion of Figure 7, this value has been taken as 1.6 for all metals and alloys.

Table 2, Table 3 and Table 5 list values of p_1, g_1, p_2, g_2, $\dot{\varepsilon}_{o1}$, and $\dot{\varepsilon}_{o1}$ used in the analyses of the metals and alloys included in these tables. It is evident that common values were selected, implying that these variables were not used as

Table A1. MTS model parameters.

Equation	Variable	Physical Constant	Independent Variable	Constrained Variable
3	μ	✓		
	μ_0	✓		
	σ_a		✓	
	$\hat{\sigma}_1$		✓	
	$\hat{\sigma}_1$		✓	
2	k	✓		
	g_{oi}		✓(g_{o1}) ✓(g_{o2})	✓($g_{o\varepsilon}$)
	b	✓		
	$\dot{\varepsilon}_{o1}$, $\dot{\varepsilon}_{o2}$			✓
	q_1, q_2			✓
	p_1, p_2			✓
4	θ_{II}		✓	
	κ			✓
5	$\hat{\sigma}_{\varepsilon so}$		✓	
	$\dot{\varepsilon}_{\varepsilon so}$			✓
	$g_{\varepsilon so}$		✓	

fitting parameters. Thus, these parameters in the "Constrained Variable" column. The same applies to values of $\dot{\varepsilon}_{\varepsilon s o}$ listed for the evolution analyses for the metals listed in Table 6 and Table 8. Indeed, $\dot{\varepsilon}_{\varepsilon s o}$ values of 10^8 s^{-1} and 10^{10} s^{-1} are both included in Table 8. However, these values greatly exceed the test strain rates and this variable is contained with a logarithmic ratio in Equation (5), which implies this difference is not significant.

The conclusion is that for a metal that can be described using a two-obstacle model, the number of independent variables listed in Table A1 is eight (8). This paper has provided further bounds for several of these variables, including g_{01}, g_{02}, and θ_{II}.